Tuning SPT-3G transition-edge-sensor electrical properties with a four-layer Ti-Au-Ti-Au thin-film stack

F. W. Carter[a,b] · P. A. R. Ade[c] · Z. Ahmed[d,e,f] · A. J. Anderson[g,b] ·
J. E. Austermann[h] · J. S. Avva[i] · R. Basu Thakur[b] · A. N. Bender[a,b] ·
B. A. Benson[g,b,j] · J. E. Carlstrom[b,k,l,a,j] · T. Cecil[a] · C. L. Chang[a,b,j] ·
J. F. Cliche[m] · A. Cukierman[i] · E. V. Denison[h] · T. de Haan[i] · J. Ding[n]
· R. Divan[o] · M. A. Dobbs[m,p] · D. Dutcher[b,l] · W. Everett[q] · A. Foster[r] ·
R. N. Gannon[n] · A. Gilbert[m] · J. C. Groh[i] · N. W. Halverson[q,s] ·
A. H. Harke-Hosemann[t,a] · N. L. Harrington[i] · J. W. Henning[b] · G. C. Hilton[h] ·
W. L. Holzapfel[i] · N. Huang[i] · K. D. Irwin[d,e,f] · O. B. Jeong[i] ·
M. Jonas[g] · T. Khaire[n] · A. M. Kofman[u,t] · M. Korman[r] · D. Kubik[g]
· S. Kuhlmann[a] · C. L. Kuo[d,e,f] · V. Kutepova[o] · A. T. Lee[i,v] · A. E. Lowitz[b] ·
S. S. Meyer[b,k,l,j] · D. Michalik[w] · C. S. Miller[o] · J. Montgomery[m] · A. Nadolski[t]
· T. Natoli[x] · H. Nguyen[g] · G. I. Noble[m] · V. Novosad[n] · S. Padin[b] ·
Z. Pan[b,l] · J. Pearson[n] · C. M. Posada[n] · A. Rahlin[g,b] · J. E. Ruhl[r] ·
L. J. Saunders[a,b] · J. T. Sayre[q] · I. Shirley[i] · E. Shirokoff[b,j] ·
G. Smecher[y] · J. A. Sobrin[b,l] · L. Stan[o] · A. A. Stark[z] · K. T. Story[d,e] ·
A. Suzuki[i,v] · Q. Y. Tang[b,j] · K. L. Thompson[d,e,f] · C. Tucker[c] ·
L. R. Vale[h] · K. Vanderlinde[x,aa] · J. D. Vieira[t,u] · G. Wang[a] ·
N. Whitehorn[bb,i] · V. Yefremenko[a] · K. W. Yoon[d,e,f] · M. R. Young[aa]

[a]Argonne National Laboratory, High-Energy Physics Division, 9700 S. Cass Ave., Argonne, IL 60439 · [b]Kavli Institute for Cosmological Physics, Univ. of Chicago, 5640 S. Ellis Ave., Chicago, IL 60637 · [c]School of Physics and Astronomy, Cardiff Univ., Cardiff CF24 3YB, United Kingdom · [d]Kavli Institute for Particle Astrophysics and Cosmology, Stanford Univ., 452 Lomita Mall, Stanford, CA 94305 · [e]Dept. of Physics, Stanford Univ., 382 Via Pueblo Mall, Stanford, CA 94305 · [f]SLAC National Accelerator Laboratory, 2575 Sand Hill Rd., Menlo Park, CA 94025 · [g]Fermi National Accelerator Laboratory, MS209, P.O. Box 500, Batavia, IL 60510-0500 · [h]National Institute of Standards and Technology, 325 Broadway, Boulder, CO 80305 · [i]Dept. of Physics, Univ. of California, Berkeley, CA 94720 · [j]Dept. of Astronomy and Astrophysics, Univ. of Chicago, 5640 S. Ellis Ave., Chicago, IL 60637 · [k]Enrico Fermi Institute, Univ. of Chicago, 5640 S. Ellis Ave., Chicago, IL 60637 · [l]Dept. of Physics, Univ. of Chicago, 5640 S. Ellis Ave., Chicago, IL 60637 · [m]Dept. of Physics, McGill Univ., 3600 Rue University, Montreal, Quebec H3A 2T8, Canada · [n]Argonne National Laboratory, Material Science Division, 9700 S. Cass Ave., Argonne, IL 60439 · [o]Argonne National Laboratory, Center for Nanoscale Materials, 9700 S. Cass Ave., Argonne, IL 60439 · [p]Canadian Institute for Advanced Research, CIFAR Program in Cosmology and Gravity, Toronto, ON, M5G 1Z8, Canada · [q]CASA, Dept. of Astrophysical and Planetary Sciences, Univ. of Colorado, Boulder, CO 80309 · [r]Physics Dept., Case Western Reserve Univ., Cleveland, OH 44106 · [s]Dept. of Physics, Univ. of Colorado, Boulder, CO 80309 · [t]Astronomy Dept., Univ. of Illinois, 1002 W. Green St., Urbana, IL 61801 · [u]Dept. of Physics, Univ. of Illinois, 1110 W. Green St., Urbana, IL 61801 · [v]Physics Division, Lawrence Berkeley National Laboratory, Berkeley, CA 94720 · [w]Univ. of Chicago, 5640 S. Ellis Ave., Chicago, IL 60637 · [x]Dunlap Institute for Astronomy and Astrophysics, Univ. of Toronto, 50 St George St, Toronto, ON, M5S 3H4, Canada · [y]Three-Speed Logic, Inc., Vancouver, B.C., V6A 2J8, Canada · [z]Harvard-Smithsonian Center for Astrophysics, 60 Garden St., Cambridge, MA 02138 · [aa]Dept. of Astronomy and Astrophysics, Univ. of Toronto, 50 St George

Abstract We have developed superconducting Ti transition edge sensors with Au protection layers on the top and bottom for the South Pole Telescope's third-generation receiver (a cosmic microwave background polarimeter, due to be upgraded this Austral Summer of 2017/2018). The base Au layer (deposited on a thin Ti glue layer) isolates the Ti from any substrate effects; the top Au layer protects the Ti from oxidation during processing and subsequent use of the sensors. We control the transition temperature and normal resistance of the sensors by varying the sensor width and the relative thicknesses of the Ti and Au layers. The transition temperature is roughly six times more sensitive to the thickness of the base Au layer than to that of the top Au layer. The normal resistance is inversely proportional to sensor width for any given film configuration. For widths greater than five micrometers the critical temperature is independent of width.

Keywords SPT-3G, Transition Edge Sensor, Proximity Effect

1 Introduction

The South Pole Telescope (SPT) is a 10 meter microwave telescope located at Amundsen-Scott South Pole Station. Its primary mission is to survey the cosmic microwave background. In the austral summer of 2016/2017 the SPT received an upgraded optical system and focal plane (known as SPT-3G). For an excellent overview of the telescope, its science goals, and the latest results from the new receiver, see Anderson, et al. (2017) in this issue [1].

The SPT-3G focal plane consists of ten six-inch wafers, each with 271 tri-chroic, polarization-sensitive pixels. To measure three frequency bands and two polarizations, each pixel has six transition-edge sensor (TES) detectors. Throughout the first year of on-sky operation, performance data from the telescope provided tighter constraints on the required TES critical temperature (T_c) and normal resistance (R_N). A new focal plane array was fabricated at Argonne National Laboratory (ANL) with TESs designed to meet these requirements. The four-layer geometry (Ti/Au/Ti/Au) of those TESs is the subject of this article. In brief, the top Au layer protects the superconducting Ti film during wafer processing and telescope operation. The base Au layer isolates the Ti from the substrate, as evidenced by reduced scatter in Tc from wafer to wafer and a decrease in transition width by a factor of 10 [2]. The bottom Ti layer (5 nm) serves as a glue layer to promote adhesion of the Au to the substrate. We discuss the tuning of both the TES T_c and R_N by varying the different layer thicknesses and the TES width. For a discussion of the fabrication of the new focal plane wafers for the 2018 observing season see Posada, et al. (2017) in this issue [3].

2 Constraints on critical temperature and normal resistance

There are four primary constraints that drive the choice of T_c and R_N: intrinsic detector noise, readout crosstalk, detector stability, and detector saturation power. Figure 1 gives an overview of these constraints.

To calculate detector noise (depicted as a background color-gradient in Fig. 1) we use the equations from [4, Sec. 2.6] for fundamental detector noise contributions (in the linear approximation) and modify them by a factor of $\sqrt{2}$ to account for an AC bias as described in [5, Appendix A]. The photon noise floor of 55 aW/$\sqrt{\text{Hz}}$ was calculated by adding the

St, Toronto, ON, M5S 3H4, Canada · [bb]Dept. of Physics and Astronomy, Univ. of California, Los Angeles, CA 90095

Constraints on T_c and R_N
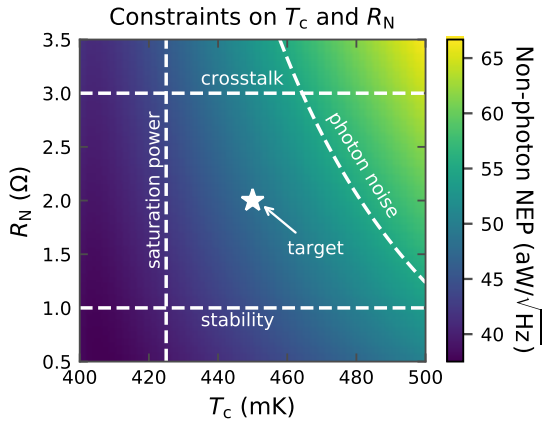
Fig. 1 Visualization of parameter phase space for TES T_c and R_N. Background color indicates total detector NEP (thermal, electrical, and an expected readout noise of 10 pA/$\sqrt{\text{Hz}}$) excluding contributions from photon noise. White dashed lines indicate boundary constraints in the parameter space that are set by various physical processes. The white star labeled "target" is the optimal combination of T_c and R_N given existing constraints and fabrication tolerances.

expected photon shot noise and expected correlation noise in quadrature for a 30 GHz wide observation band centered at 150 GHz. The white dashed line in Fig. 1 labeled "photon noise" delineates the region of phase space where the detector noise level is below this floor.

The TES stability requirements are calculated from [4, Sec. 2.4] and are constrained by our choice of readout electronics. We frequency-multiplex our detectors by wiring each TES in series with an inductor-capacitor resonator. The width of each resonance is primarily set by the TES R_N; higher resistances equate to broader resonance peaks. Although a higher resistance can be good for detector stability, it increases noise, and too large of a resistance results in an overly broad peak that can leak into the neighboring readout channels. For more information, see [5, Eq. (8)]. The crosstalk and stability constraints depicted in Fig. 1 reflect specific choices made regarding readout electronics that are unique to our focal plane.

The 275 mK base temperature of the SPT-3G cryostat sets a hard lower limit on the allowed T_c. The TES saturation power (the maximum incident photon power before the detector is driven normal), which should be $\approx$2 times the optical loading from the telescope, adjusts this limit upwards to about 425 mK. The saturation power limit was calculated assuming a fixed thermal conductivity between the TES and the bath.

3 Methods

3.1 Measurement and fabrication of test structures

We fabricated many isolated four-layer Ti/Au/Ti/Au film test structures with various combinations of each layer's thickness (except the bottom Ti glue layer, which was always 5 nm). The test structure geometry was designed to be the same length as a SPT-3G TES, but with several different widths. Each four-layer sample was fabricated in the same sputtering chamber used for production SPT-3G wafers, and all four film layers were deposited without breaking vacuum. The design of the test structures included pads for wirebonding directly to the sample to avoid the need for depositing leads for readout. Unlike the TESs on production SPT-3G wafers, these test films were not suspended on a SiN membrane, but deposited directly on a SiN-coated Si substrate.

The samples were mounted in a light-tight box and cooled down in an High Precision Devices Olympus adiabatic demagnetization refrigerator (ADR). The temperature was

swept over the superconducting transition by ramping the magnetic field applied to the ADR salt pills to maintain an approximate heating rate of 15 mK/hr, which was sufficiently slow to minimize hysteresis in the T_c. Four-wire resistance measurements were performed with a Lakeshore LS372 AC bridge operating at $\approx$13 Hz. The LS372 has two simultaneous readout channels (readout and monitor). We used a four-wire switch to multiplex 12 samples onto the readout channel, and monitored temperature with a calibrated germanium thermometer. Excitation current ranged from 100 nA to 1 μA, but care was taken to ensure that the excitation level was low enough so as not to bias the measurement.

3.2 Measurements of candidate SPT-3G wafers

For reading out entire SPT-3G wafers (each with $\approx$1500 membrane-suspended TES detectors) we use a frequency-domain-multiplexing readout system called Dfmux, which combines 68 detectors on one pair of wires. A detailed description is available in [5,6].

Because the transfer function that maps Dfmux output (ADC bits) to actual currents and voltages present across the TES is complicated, depends on frequency, and is not well characterized for absolute measurements of resistance, we do not expect to get precise values for R_N. However, T_c measurements are accurate provided the optical loading on the wafer is minimized. This second condition is nearly true for our so-called "dark" testbeds where the wafer primarily sees a metal plate that is at wafer temperature. Each wafer contains several dark pixels that lack the termination resistor that couples antenna power into the bolometer. These pixels should give a nearly correct T_c regardless of loading conditions. However, in practice we still notice a small difference in T_c between the 90 GHz and 220 GHz dark pixels, which suggests that there is still some minor loading. As the 220 GHz bolometers have the largest saturation power, they should give the most accurate value for a true unloaded T_c and so where T_c is quoted for an optical wafer, the value quoted is that of a dark 220 GHz TES.

We also measured several individual membrane-suspended TESs from SPT-3G wafers in the same four-wire setup described in section 3.1. This necessitated breaking a full wafer into individual pixels, wirebonding directly to test pads included next to each TES, and mounting them in the ADR. This was done to verify that the full-wafer T_c measurements matched those of the test-structures for at least a small sampling of film geometries.

4 Results and analysis

In Fig. 2 we plot the T_c of each sample (or wafer) as a function of the Ti layer thickness. In all cases, T_c was calculated as the temperature at which the sample resistance was $R_N/2$. Results are displayed in a matrix of plots where the columns (left to right) correspond to increasing base-layer Au thickness, and the rows (top to bottom) correspond to increasing top-layer Au thickness. Test structure sample data is depicted as colored circles where the color denotes the year the Ti sputter target was purchased (the volume of fabrication over the course of three years was sufficient to require multiple target replacements—all three targets were nominally identical). Red triangles, pink inverted triangles, and yellow stars denote measurements of TESs on SPT-3G candidate wafers (see caption for details). There is a systematic offset in T_c of actual measured wafers as compared to test samples for nearly all of the wafer measurements except for those from broken wafers measured using the four-wire technique (pink inverted triangles). This suggests some combination of excess loading and/or unidentified systematics in our Dfmux readout system.
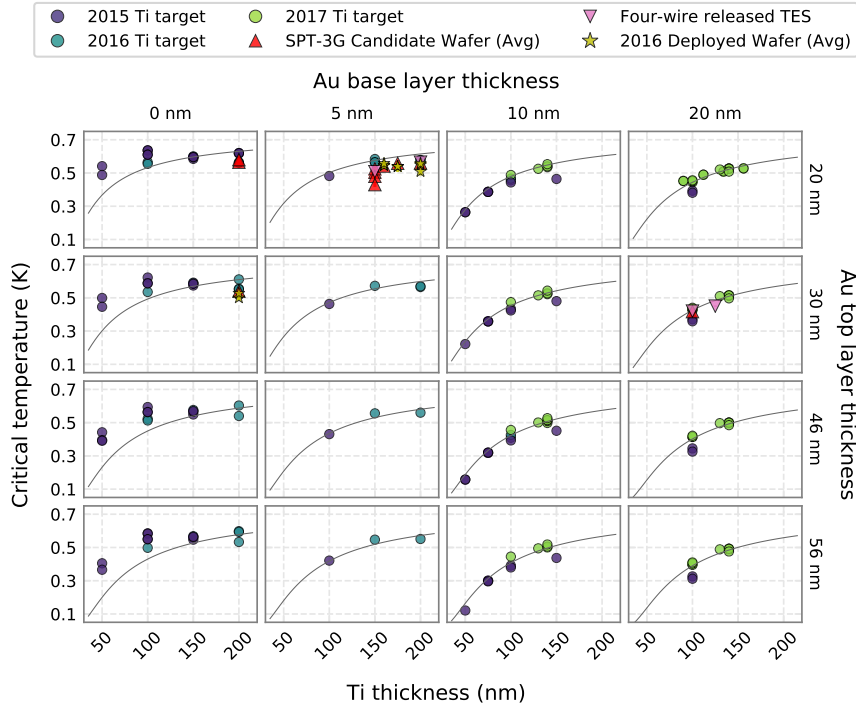
Fig. 2 Matrix of results of T_c measurements of samples grouped by common dimensions of top/base layer Au thickness. Base Au thickness increases from left to right and top Au thickness increases from top to bottom. *Circular* data points represent samples measured in a four-wire test setup and are colored by which Ti target was used to make them. *Red triangles* are Dfmux measurements of dark 220 GHz detectors on SPT-3G candidate wafers. *Inverted pink triangles* are four-wire measurements of TESs from SPT-3G candidate-wafers that were broken into individual pixels for four-wire testing. *Yellow stars* are Dfmux measurements of dark 220 GHz detectors on wafers installed in the SPT-3G focal plane during the austral summer of 2016/2017. *Solid lines* are model fits to the circular data points; all data were fit simultaneously. TES samples with different widths are all plotted together as the effects of width on T_c are minimal (see Fig. 3).

The solid lines are least-squares fits of a proximity effect model to the test sample data (circles) where we weighted the residual of each sample by that sample's transition width (2–37 mK for $d_{Au}^{base} = 0$ nm and 0.5–5 mK for $d_{Au}^{base} > 0$ nm). A full model requires solving the Usadel equations for a tri-layer. However, we can develop a preliminary quantitative description of our results by using the model from [7, Eqs. (25) and (30)] that calculates the T_c of a superconducting/normal bilayer and adapting it to our four-layer geometry as follows: we neglected the effects of the Ti glue layer and reasoned that two layers of Au should perform analogously to a single, thicker layer. Because the base Au layer seems to depress T_c much more strongly than the top layer does, we used an effective single layer thickness $d_{Au}^{eff} = w d_{Au}^{base} + d_{Au}^{top}$ where the weighting factor (w) applied to the thickness of the base layer is a free parameter to allow the two thicknesses to independently suppress T_c. This parameterization allows us to quantify our results directly using the bilayer calculations in [7]. The only other free parameter in the model was a unitless interface transparency
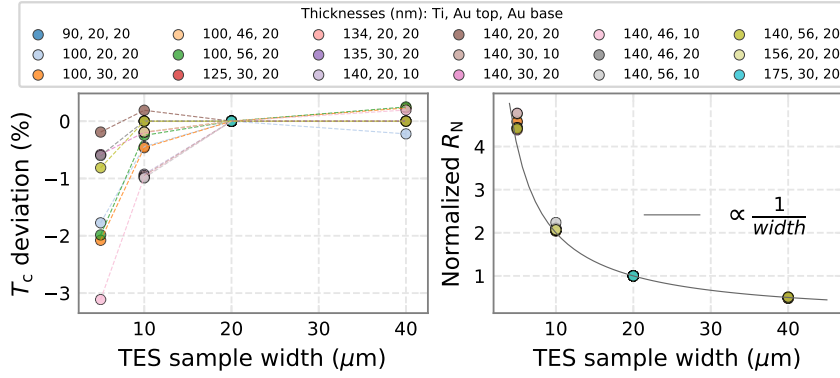
Fig. 3 The effects of sample width on T_c and R_N. Each *color* denotes one of 18 unique sets of four-layer film dimensions (see legend for details), each containing samples of several different widths. The *left* panel shows the percent-deviation of sample T_c from the T_c of the 20 μm wide sample in each set (*dashed lines* are a guide to the eye). The *right* panel shows the R_N of each sample at several different widths, normalized by the resistance of the 20 μm wide sample in each set. The *solid line* shows a 1/*width* dependence (not a fit), which describes the data very well. Twenty microns was chosen as the comparison width as it was the only width that all 18 sets of films shared. Each plot shows 49 data points.

describing the quality of the boundaries between films in the bi-layer, which are assumed to be identical. We neglected the effects of the Ti glue layer in this model.

This model reproduces the behavior of our tests modulo some systematic offset between target years. The best-fit value for the weight factor (when fitting all test sample data simultaneously) is $w = 1.4$. An equivalent statement is: "a given base layer thickness seems to depress T_c the same as a top layer that is 1.4 times thicker".

In Fig. 3 we plot both the T_c and the R_N of many test samples as functions of sample width. In each plot we group samples of different widths that share identical film thicknesses by color, and then normalize by the value of the 20 μm sample. In the left panel we show the percent deviation of T_c and in the right panel we show the normalized R_N. In both cases T_c decreases only slightly as sample width narrows and R_N varies inversely with sample width.

5 Conclusions

In summary, we reiterate the following four points: 1. We can both control and predict the T_c of our TESs (± 20 mK) by adjusting film thicknesses in accordance with our modified bilayer model; 2. We can independently control the R_N of our TESs by varying their widths, provided all widths are greater than five micrometers; 3. The top layer of Au appears to be less effective than the base layer in suppressing T_c. This is not something we currently understand, but we offer two hypotheses: either the Ti/Au interfaces between the top and base layers of Au may differ in quality or the weight factor should perhaps depend on total gold thickness rather than being constant; and 4. The dominant systematic uncertainty in our ability to predict T_c seems to be the Ti sputter target. Alternatively this could be a statement about the drift of our entire system over time. Regardless, the result strongly suggests that it is crucial to re-characterize the system baseline at regular intervals and update the model used for T_c prediction.

References

1. A.J. Anderson, P.A.R. Ade, Z. Ahmed, et al., Journal of Low Temperature Physics **LTD-17, Abstract number O-69** (2017)
2. J. Ding, P.A.R. Ade, A.J. Anderson, et al., IEEE Transactions on Applied Superconductivity **27**(4) (2017). doi:10.1109/TASC.2016.2639378
3. C.M. Posada, P.A.R. Ade, Z. Ahmed, et al., Journal of Low Temperature Physics **LTD-17, Abstract number PC-23** (2017)
4. K.D. Irwin, G.C. Hilton, C.E. Ed, *Transition-Edge Sensors - a chapter in Cryogenic Particle Detection*, vol. 99 (2005). doi:10.1007/10933596_3
5. M.A. Dobbs, M. Lueker, K.A. Aird, et al., Review of Scientific Instruments **83**(7), 1 (2012). doi:10.1063/1.4737629
6. A.N. Bender, P.A.R. Ade, A.J. Anderson, et al., SPIE 9914, Millimeter, Submillimeter, and Far-Infrared Detectors and Instrumentation for Astronomy VIII **9914**, 99141D (2016). doi:10.1117/12.2232146
7. Y.V. Fominov, M.V. Feigel'man, Phys. Rev. B **63**(February), 094518 (2001). doi:10.1103/PhysRevB.63.094518